

Broadening of the Divertor Heat Flux Profile in High Confinement Tokamak Fusion Plasmas with Edge Pedestals Limited by Turbulence in DIII-D

D. R. Ernst,¹ A. Bortolon,² C. S. Chang,² S. Ku,² F. Scotti,³ H. Q. Wang,⁴
Z. Yan,⁵ Jie Chen,⁶ C. Chrystal,⁴ F. Glass,⁴ S. Haskey,² R. Hood,⁷ F. Khabanov,⁵
F. Laggner,⁸ C. Lasnier,³ G. R. McKee,⁵ T. L. Rhodes,⁶ D. Truong,⁷ and J. Watkins⁷

¹Massachusetts Institute of Technology, Cambridge, Massachusetts, 02139*

²Princeton University Plasma Physics Laboratory, Princeton, NJ 08840

³Lawrence Livermore National Laboratory, Livermore, CA 94550

⁴General Atomics, San Diego, CA 92121

⁵University of Wisconsin, Madison, WI 53715

⁶University of California, Los Angeles, CA 90095

⁷Sandia National Laboratory, Livermore, CA 94551

⁸North Carolina State University, Raleigh, NC 27695

(Dated: March 21, 2024)

Multi-machine empirical scaling predicts an extremely narrow heat exhaust layer in future high magnetic field tokamaks, leading to disastrous damage. In the experiments presented, the width of this exhaust layer is nearly doubled by using actuators to increase turbulent transport in the plasma edge. This is achieved in low collisionality, high confinement edge pedestals with their gradients limited by turbulent transport instead of large-scale, coherent instabilities. The exhaust heat flux profile width and divertor leg diffusive spreading both double as a high frequency band of fluctuations propagating in the electron diamagnetic direction doubles in amplitude. The results are quantitatively reproduced in comprehensive electromagnetic XGC particle-in-cell simulations which show the heat flux carried by electrons emerges to broaden the heat flux profile.

The tokamak is the main approach being pursued worldwide toward magnetic fusion energy production. It confines a plasma in a toroidal magnetic field, typically several Tesla, created by external solenoidal coils with a helical twist added by the toroidally flowing plasma current. The magnetic field lines lie on nested, closed flux surfaces. The fusion power produced is proportional to the square of the core plasma pressure. Achieving high pressure requires good energy confinement, most often achieved by creating a narrow edge transport barrier where densities and temperatures rise sharply just inside the last closed flux surface (LCFS). Referred to as High Confinement Mode (H-Mode), the edge transport barrier forms a “pedestal” which raises the entire pressure profile, approximately doubling the global energy confinement time. The H-Mode pedestal formation is aided by using external coils to create a magnetic “X-point” at the LCFS where the poloidal magnetic field vanishes, as shown in Fig. 3. The X-point prevents magnetic field lines outside the LCFS from closing, causing them to be diverted to either side of the X-point. These open field lines then terminate on plates in the “divertor”, which acts as a receptacle for the particle exhaust. Particles from the core which cross the LCFS stream down the open magnetic field lines to the divertor at the sound speed. While the magnetic field lines are spread further apart in the divertor, the heat load from the particle exhaust is still concentrated in a narrow toroidal annulus on the divertor plates. Further, in conventional H-Modes, the pedestal pressure and plasma current density rise until an edge stability limit is reached, resulting in

frequent, periodic Edge Localized Mode (ELM) crashes which dump large bursts of energy and particles into the divertor. Both the steady and transient components of this heat load can reach tens of MW/m², potentially exceeding thermal stress limits and melting or eroding plasma facing components. Mitigating the plasma exhaust heat load remains one of the great challenges for the tokamak approach.

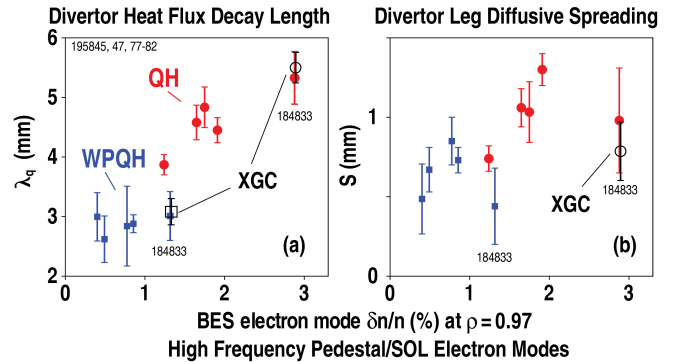


FIG. 1. (a) Measured λ_q from Langmuir Probes (LP) for discharges varying the plasma current from 0.7 to 1.3 MA, as a function of BES measured high-frequency electron mode density fluctuation amplitude $\delta n/n$ at $\rho = 0.97$, and (b) Corresponding measured divertor leg diffusive spreading S . Results from XGC simulations are shown in black open symbols with x -coordinates artificially adjusted to match measured values for #184833 (noise prevents determination of S from XGC for WPQH). Error bars represent statistical standard deviations in the time averages. Definitions of λ_q and S are given in the Appendix.

Macroscopic stability limits the ratio of plasma pressure to magnetic pressure, so that stronger magnetic fields enable access to higher pressures and thus higher fusion power. However, multi-machine empirical scaling [1, 2] would predict the exhaust heat flux width depends inversely on (poloidal) magnetic field, so that stronger magnetic fields lead to more concentrated divertor heat loads. For example, the scaling predicts a midplane width $\lambda_q \lesssim 1$ mm for the heat exhaust layer of the ITER tokamak, now under construction. The scaling is consistent with the heat flux being carried mainly by the ions, mediated by finite ion orbit width effects [3].

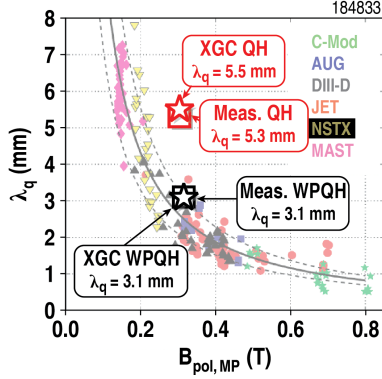


FIG. 2. Comparison of divertor heat flux widths λ_q from XGC simulations with measurements, for WPQH-mode and Turbulent QH-Mode, against the multi-machine Eich scaling [2] (DIII-D #184833).

In this Letter we demonstrate experimentally that the divertor heat flux width (referred to the outer midplane) λ_q increases with the intensity of high frequency turbulence propagating in the electron diamagnetic direction near the last closed flux surface. We show that for Quiescent H-Mode plasmas in the DIII-D tokamak where edge turbulence is sufficiently strong, λ_q does not follow the empirical scaling, and can even increase favorably with poloidal magnetic field. In these experiments we have used actuators (varying applied toroidal torque and plasma current) to control the edge turbulence. Multiple diagnostic measurements of both edge turbulence and divertor heat flux profiles show that as the electron turbulence intensifies, the fraction of the divertor heat flux carried by electrons increases and its profile broadens, broadening the total heat flux profile. The endpoints of the measured λ_q range are quantitatively matched within measurement uncertainty by XGC gyrokinetic particle simulations, as summarized in Figs. 1 and 2. The mechanism for the broadening identified in these experiments lends plausibility to analogous XGC predictions of $\lambda_q \sim 6$ mm for ITER [4, 5].

In addition to the doubling of λ_q shown, there are no ELMs in these Quiescent H-Mode (QH-Mode) plasmas, which maintain steady high energy confinement with turbulent transport limiting pedestal gradients. Broadening of λ_q has also been observed in the Quasi-Continuous

Exhaust (QCE) or small ELM regime on the ASDEX Upgrade tokamak with increased fueling [6–8], where it was associated with filamentary transport near the LCFS, thought to be driven by resistive ballooning modes (RBM), though turbulence measurements providing evidence for RBM being the cause are not yet available. The QCE regime operates with high edge collisionality (ratio of trapped electron collision frequency to bounce frequency, $\nu_{*e} > 10$) which is beneficial for detaching the divertor (dissipating the heat flux by radiation), but it is not clear if ITER will be able to access the necessary onset conditions for QCE. Because future machines will operate at high temperatures and thus low collisionality at the pedestal top, our results are obtained with pedestal top collisionality $\nu_{*e} \sim 0.1$ similar to that expected in ITER regimes predicted to reach the goal of $Q=10$ fusion gain. This low collisionality increases the pedestal gradient-driven bootstrap current, resulting in operation near the stability boundary for current-driven peeling modes rather than pressure gradient driven ballooning modes. Overall, we show the width of the exhaust layer in turbulence-limited QH-Modes does not follow the empirical scaling with poloidal magnetic field B_p (T) at the outer midplane, $\lambda_q^{Eich} = 0.63 B_p^{-1.19}$. We argue that turbulence will be much stronger in future pedestals at higher magnetic field, which may naturally prevent ELM transients while offering relief from the extreme steady divertor heat loads predicted by empirical scaling.

Figure 3 shows the temporal evolution for the case #184833 exhibiting the greatest broadening, shown in Fig. 1. We first establish an H-Mode edge pedestal limited by turbulent transport without ELMs, exhibiting a high and wide pedestal pressure profile, referred to as the Wide Pedestal Quiescent H-Mode (WPQH-Mode) regime [9–12]. Its pedestal width (edge transport barrier width) in normalized poloidal magnetic flux significantly exceeds that predicted by EPED scaling [13, 14], given by $0.089 \beta_p^{1/2}$, where $\beta_p = 8\pi p / B_p^2$ is the pedestal top ratio of kinetic pressure to magnetic pressure. This regime is accessed through wall conditioning (boronization) to reduce collisionality, and low neutral beam injected (NBI) toroidal torque < 2 Nm. During the period 4–5 s the counter- I_p NBI torque is increased from 0.6 Nm to 4 Nm, provoking a back-transition to a little explored variant of Standard Quiescent H-Mode (QH-Mode) which exhibits only broadband pedestal turbulence [15], referred to here as Turbulent QH-Mode. The energy confinement time, pedestal pressure, and pedestal width step down significantly at this transition, indicating increased turbulent transport. The lower divertor heat flux profiles are measured by fixed Langmuir probes and infra-red (IR) camera imaging using strike point sweeps in each phase. Close agreement between Langmuir probes and IR thermography is found when using the standard sheath heat flux transmission coefficient to relate total parallel heat

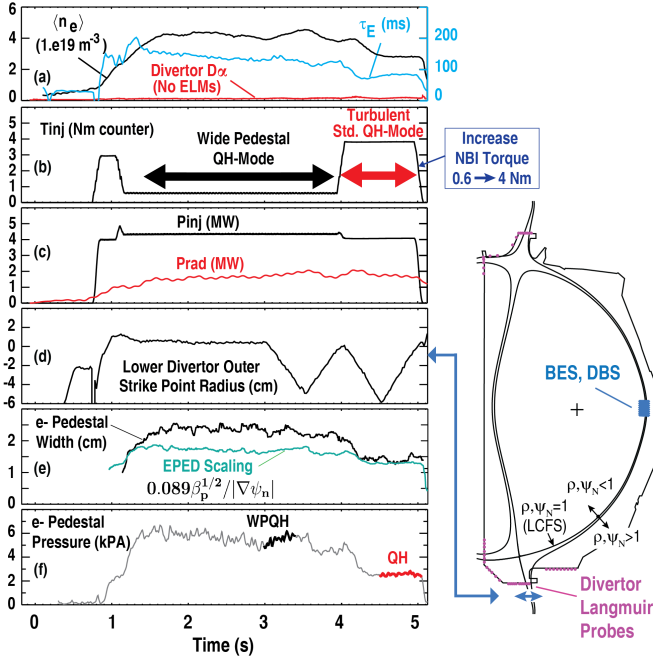


FIG. 3. Evolution of (a) plasma density, energy confinement time τ_E , and Divertor $D\alpha$ emission, (b) neutral beam torque T_{inj} counter to the plasma current, (c) injected neutral beam power P_{inj} and radiated power P_{rad} , (d) lower divertor outer strike point major radius, (e) width of electron edge pedestal pressure relative to EPED scaling (ψ_n is the poloidal magnetic flux enclosed normalized to its LCFS value), (f) electron pedestal top pressure (averaging time windows for analysis of WPQH/QH-Mode phases shown).

flux to Langmuir probe measured electron saturation current and electron temperature [16]. The comparison, together with detailed measurements for all discharges are given in the Appendix.

The increased pedestal energy transport and broadened (λ_q, S) in Turbulent QH-Mode are accompanied by a pronounced increase in high frequency density fluctuation amplitudes measured by Beam Emission Spectroscopy (BES) [17]. As shown in Fig. 4(a,b), two distinct features are observed, a lower frequency band of fluctuations propagating in the ion diamagnetic direction (~ 7 to 50-100 kHz), and a higher frequency band of fluctuations above 50-100 kHz propagating in the electron diamagnetic direction in the laboratory frame, as shown in Figs. 4(c, d). The low frequency ion-directed fluctuations reach maximum intensity near the magnetic LCFS ($\rho \sim 1$) with relatively little change in intensity in the transition from WPQH-Mode to QH-Mode (the calibration is not as reliable for $\rho > 1$). On the other hand, the measured high frequency electron-directed fluctuations in the pedestal triple in amplitude in QH-Mode relative to WPQH-Mode. For reference, the increased shear in the parallel flow due to the increased injected torque has been shown to increase the drive for trapped electron modes (TEMs) in the QH-Mode core [18]. Measure-

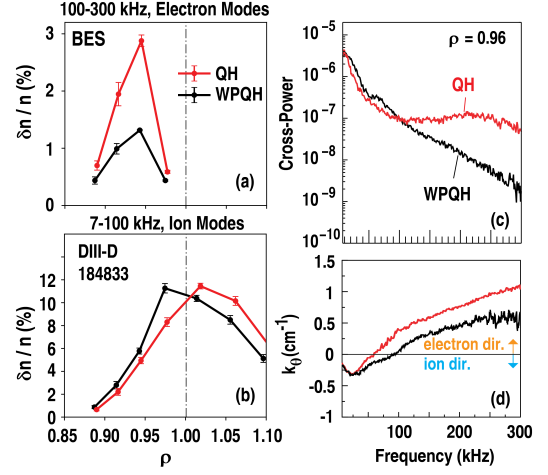


FIG. 4. Pedestal radial profiles of normalized density fluctuation amplitude measured by Beam Emission Spectroscopy (BES), for WPQH-Mode and (BB)QH-Mode phases, for turbulence propagating in the lab frame (a) electron, and (b) ion diamagnetic directions, with (c) BES cross-power and (d) cross-phase (k_θ frequency spectra for vertically adjacent channels, showing modes in the ion (electron) diamagnetic direction at low (high) frequencies, at radial location $\rho = 0.96$ corresponding to the peak $\delta n/n$ in (b). Here ρ is the minor radial coordinate given by the square root of toroidal magnetic flux enclosed, normalized to its value at the LCFS.

ment of the high frequency electron-directed fluctuations around the LCFS is not available for this XGC-simulated discharge, but available in the other more recent discharges shown. Fig. 5(a) shows the low frequency fluctuations (in most cases ion-directed) change little in the transition from WPQH-Mode to QH-Mode, even though there is a doubling of λ_q . This is an indication that the ion-directed fluctuation is not related to the widening of λ_q . The low frequency amplitudes are comparable to the higher frequency electron directed fluctuations and much weaker than #184833. The stronger electron fluctuations in QH-Mode measured by BES are confirmed in separate Doppler Backscattering (DBS) measurements, shown in Fig. 5(b), selecting shorter poloidal wavelengths than BES, $k_\theta \sim 3 - 5 \text{ cm}^{-1}$, $k_\theta \rho_s \sim 1$, and toroidal mode numbers $N \sim 30 - 50$, where $\rho_s = (T_e/m_i)^{1/2}/\Omega_{ci}$ is the ion sound gyroradius with $\Omega_{ci} = ZeB/m_i c$ the ion cyclotron frequency. The DBS measurements show the same large relative change in density fluctuation levels in the WPQH to QH-Mode transition. Unlike the discharge #184833, here the electron-direction fluctuations are measurable by BES at $\rho \sim 1$ for several similar cases, extending outside the LCFS. A case with 1.1 MA plasma current is shown in Fig. 5(a) as an example.

These results are further confirmed in a plasma current scan (over the range 0.7 to 1.3 MA). While the λ_q values measured in WPQH-Mode are consistent with the multi-machine Eich scaling [2], λ_q in Turbulent QH-Mode exhibits a more complex, favorable, non-monotonic variation with B_p , as shown in Fig. 6(a). This non-monotonic

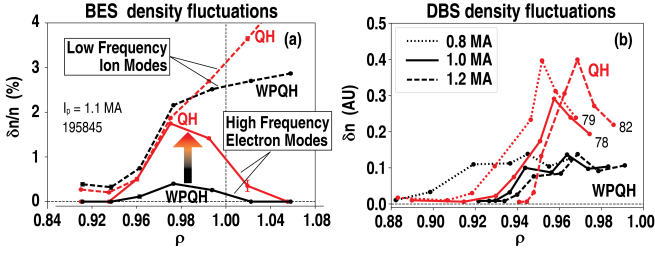


FIG. 5. (a) BES measurements of density fluctuations, showing lab frame ion-directed low frequency ($\lesssim 50 - 90$ kHz) modes at and high frequency ($\gtrsim 50 - 90$ kHz) electron-directed modes for both WPQH and QH phases, and (b) DBS measured δn radial profiles for shorter wavelength modes in the range $k_\theta \sim 3 - 5 \text{ cm}^{-1}$, $k_\theta \rho_s \sim 1$, and toroidal mode number $N \sim 30 - 50$, generally corresponding to electron modes, comparing WPQH and QH phases for three plasma currents for discharges (discharges #195879, 78, 82) matched to 195845 in (a).

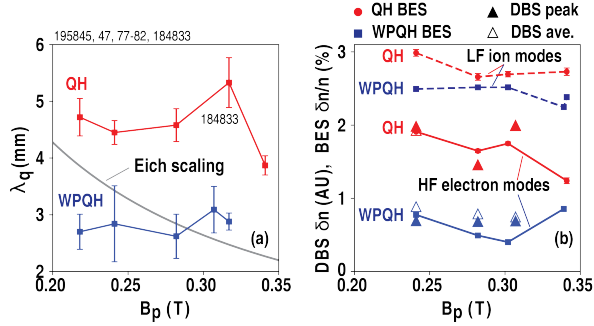


FIG. 6. Results of a recent plasma current scan: (a) Measured λ_q values from Langmuir probes as a function of outer midplane poloidal magnetic field at the LCFS, B_p , and (b) Measured density fluctuation amplitudes from BES for high frequency ($\gtrsim 50 - 90$ kHz) modes in the electron direction at $\rho = 0.97$, and for low frequency ($\lesssim 50 - 90$ kHz) modes propagating in the ion diamagnetic direction at $\rho = 1.0$ (near the maximal amplitude), together with DBS measurements of electron-directed δn showing the peak value and the average of the outermost 5 radial points (see also Fig. 5).

variation is reorganized as a monotonic increase with density fluctuation level in Fig. 1. The density fluctuation amplitudes shown for high frequency electron modes in Fig. 6(b) show similar behavior to that of λ_q in (a). Density-weighted, radially line-integrated fluctuations of the fluctuating magnetic field, δB_R , were measured by the radial interferometer-polarimeter (RIP) [19], and exhibit low and high frequency bands similar to BES. The high frequency band shows a Doppler shift corresponding to the pedestal and is approximately four times larger in magnitude than the low frequency band. Both bands track the density fluctuation levels from BES, with the high frequency band doubling in amplitude as the BES high frequency band of density fluctuations doubles in amplitude.

Both the WPQH-Mode and QH-Mode phases of discharge #184833 are simulated with the XGC total- f gy-

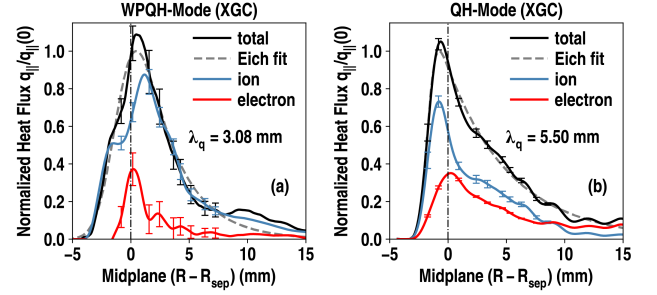


FIG. 7. XGC results for DIII-D #184833, showing the parallel heat flux at the last mesh point above the lower divertor plate, plotted against midplane major radius relative to the LCFS location, in (a) WPQH-Mode and (b) BBQH-Mode. Dashed curves show the fitted Eich function with corresponding λ_q . The contributions of ions and electrons to the total heat flux are shown separately. Error bars represent the standard deviation on the time average.

rokinetic particle code [4], using gyrokinetic ions and drift-kinetic electrons, and including Monte Carlo neutrals with recycling coefficient 0.99, the carbon impurity density as measured, and electromagnetic effects. Radial pedestal profiles used as input to XGC in the Appendix. Focusing on the electron mode turbulence, toroidal mode numbers $N = 1 - 5$ are filtered out to avoid possible MHD related fast instabilities (this may artificially reduce the lowest frequency ion-directed turbulence amplitude). The overall results for λ_q are shown in Fig. 2, overlaid on the multi-machine database [2].

We offer the following explanation for the measured λ_q broadening associated with the increased intensity of high frequency electron turbulence. The contributions in XGC simulations to the parallel heat flux at the last mesh points above the divertor plates are shown in Fig. 7 for the WPQH-Mode (a) and QH-Mode (b) cases. The WPQH-Mode heat flux width λ_q is consistent with the Eich empirical scaling value, with most of the heat flux carried by the ions. Its profile width is determined by ion magnetic drift velocity v_{di} . The Goldston heuristic model [3] yields the estimate $\lambda_q^{\text{Goldston}} \sim v_{di} qR / v_{Ti} \sim \varepsilon \rho_{\text{pol},i} \propto B_{\text{pol}}^{-1}$ where qR is the field line length from midplane to divertor, v_{Ti} is the ion thermal speed, $\varepsilon = r/R$ is the inverse aspect ratio of the torus, and $\rho_{\text{pol},i}$ is the ion gyro-radius using the poloidal magnetic field, which is consistent with the Eich scaling. The ion channel width was hypothesized to carry electron parallel heat flux [3]. For QH-Mode, the XGC simulations reveal a greater and broader electron contribution to the heat flux which emerges to broaden the total heat flux profile, associated with electron thermal transport from the higher temperature pedestal region. The increased electron thermal transport can be expected to accompany the stronger electron turbulence observed in measurements and simulations, which extends to the LCFS. TEM tur-

bulence is known to most efficiently transport electron thermal energy, particles, and impurities [18].

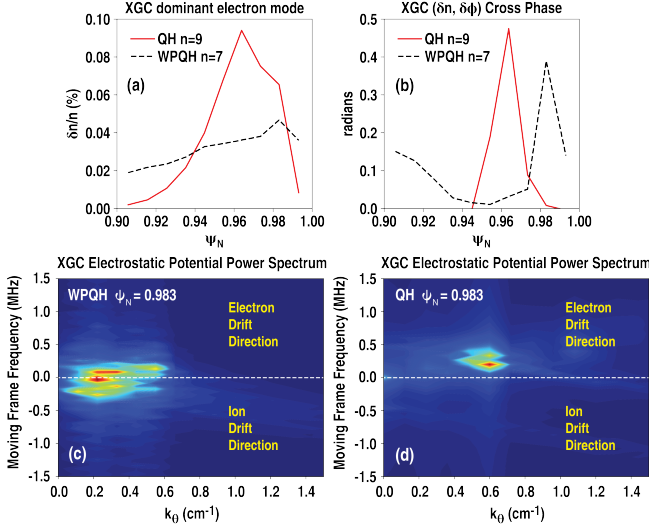


FIG. 8. (a) Density fluctuation level for the dominant electron mode in XGC simulations of #184833 for WPQH ($N = 7$) and BBQH ($N = 9$) phases, for modes propagating in the electron diamagnetic direction in the lab frame, and (b) the cross-phase between fluctuating density (δn) and electrostatic potential ($\delta \phi$) for the modes in (a); (c, d) XGC plasma frame frequency-wavenumber spectra corresponding to WPQH and BBQH phases, respectively, at $\psi_N = 0.983$.

The XGC simulations of toroidal mode number $N > 5$ modes show overall consistency with the fluctuation measurements described above. Fig. 8(a) shows $\delta n/n$ for the dominant toroidal mode number (N) fluctuations propagating in the electron direction, for WPQH-mode ($N = 7$) and QH-Mode ($N = 9$), indicating that XGC simulations find a relative increase for this toroidal mode similar to that measured in Figs. 4(a) in the steep gradient pedestal region. We have implemented synthetic BES in XGC to attempt validation of the XGC results against experimental observations at higher frequencies corresponding to $N > 5$; preliminary results nearly match the total measured BES $\delta n/n$ profile for the QH case. The corresponding cross-phase between density and potential fluctuations ($\delta n, \delta \phi$) from XGC is shown in Fig. 8(b). Noting that an “adiabatic” or Boltzmann electron density response would be in phase with the electrostatic potential, a strong non-adiabatic electron behavior (typical of the trapped electron response) is indicated by the non-zero cross-phase. This produces significant electron particle and thermal transport, typical of TEM turbulence. From XGC, the lab frame frequency of the QH fea-

ture is 330 kHz, while the poloidal wavenumber $k_\theta = 0.63$ cm⁻¹, consistent with the measurements in Fig. 4(c, d). In the plasma frame moving with the $E \times B$ velocity, the WPQH-Mode case shows both ion and electron modes spanning a range of wavenumbers, $k_\theta \sim 0.1 - 0.6$ cm⁻¹ (Fig. 8(c)), while in contrast, the QH-Mode case shows mainly electron modes with $k_\theta \sim 0.4 - 0.7$ cm⁻¹ (Fig. 8(d)).

Finally, scaling arguments based on theory and simulation suggest that in future machines, pedestal turbulent transport may be sufficiently limiting to naturally maintain stability to edge localized modes (ELMs) [10, 21] so that Non-ELMing regimes naturally arise (see Appendix for details). Intrinsically Non-ELMing operating regimes such as Wide Pedestal Quiescent H-Mode and Quiescent H-Mode offer a high-performance solution without ELMs at relevant low pedestal top collisionalities, with the added benefit of broadened divertor heat flux profiles when the pedestal turbulent transport is sufficiently strong.

This material is based upon work supported by the U.S. Department of Energy, Office of Science, Office of Fusion Energy Sciences, using the DIII-D National Fusion Facility, a DOE Office of Science user facility, under Award(s) DE-FC02-04ER54698, DE-SC0014264, DE-AC02-09CH11466, DE-SC0019004, DE-AC52-07NA27344, DE-NA0003525, DE-FG02-08ER54999, and DE-SC0019352. This research used resources of the National Energy Research Scientific Computing Center (NERSC), a U.S. Department of Energy Office of Science User Facility located at Lawrence Berkeley National Laboratory, operated under Contract No. DE-AC02-05CH11231.

Disclaimer: This report was prepared as an account of work sponsored by an agency of the United States Government. Neither the United States Government nor any agency thereof, nor any of their employees, makes any warranty, express or implied, or assumes any legal liability or responsibility for the accuracy, completeness, or usefulness of any information, apparatus, product, or process disclosed, or represents that its use would not infringe privately owned rights. Reference herein to any specific commercial product, process, or service by trade name, trademark, manufacturer, or otherwise does not necessarily constitute or imply its endorsement, recommendation, or favoring by the United States Government or any agency thereof. The views and opinions of authors expressed herein do not necessarily state or reflect those of the United States Government or any agency thereof.

Appendix

Eich Function. The integral heat flux profile width λ_{int} can be related to the Eich fit parameters (λ_q, S) by $\lambda_{\text{int}} = \int (q_{\parallel}(s) - q_{\text{BG}}) ds / (q_{\parallel 0}) \approx \lambda_q + 1.64 S$ [1]. The Eich function is given by

$$q_{\parallel}(\bar{s}) = \frac{q_{\parallel 0}}{2} \exp \left[\left(\frac{S}{2\lambda_q} \right)^2 - \frac{\bar{s}}{\lambda_q f_x} \right] \text{erfc} \left(\frac{S}{2\lambda_q} - \frac{\bar{s}}{S f_x} \right) + q_{\text{BG}} \quad (\text{A.1})$$

where $\bar{s} = s - s_0 = (R_{\text{mp}} - R_{\text{LCFS}})f_x$ is the radial coordinate at the divertor, referring to the departure in midplane major radius from the LCFS, and $f_x = R_{\text{div}} B_{\text{pol}}^{\text{div}} / R_{\text{mp}} B_{\text{pol}}^{\text{mp}} \approx 5.3$ (for our cases) is the flux expansion effective area factor from midplane to divertor. The two parameters (λ_q, S) characterize the midplane exponential decay length and the Gaussian width, referred to the midplane, where S represents competition between parallel and perpendicular heat transport between the X-point and strike point [2]. The Eich function is the convolution of an exponential decay in the scrape-off layer and a Gaussian diffusive width characterized by S . Note the IR data for these experiments has insufficient coverage to constrain S , which is obtained from Langmuir probe measurements.

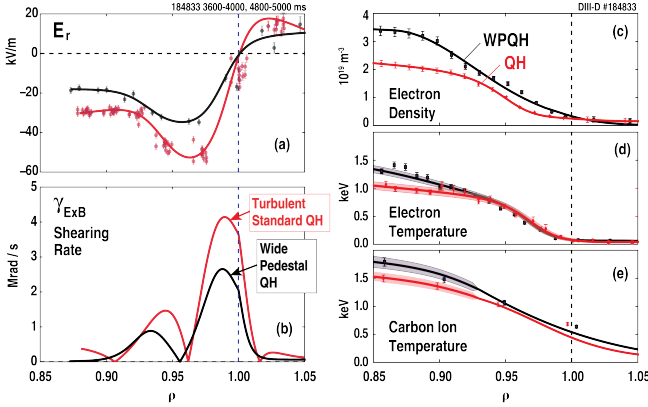


FIG. A.1. Edge radial profiles for DIII-D #184833, comparing WPQH and QH-Mode phases. (a) Radial electric field E_r , (b) Hahn-Burrell $E \times B$ shearing rate, (c) electron density, (d) electron temperature, and (e) carbon ion temperature.

Profile Fits. Pedestal profiles, shown in Fig. A.1, are constrained by Langmuir probe measurements of separatrix electron temperature T_e^{sep} and pedestal carbon and deuterium charge exchange measurements, which show constant carbon concentration across the pedestal. Equilibrium reconstructions of discharge #184833 in WPQH and QH phases, including the bootstrap current and realistic heating profiles from interpretative transport simulations (TRANSP) are used as input to the XGC code.

Divertor Heat Flux Measurements. Using the standard sheath heat transmission coefficient $\gamma_{\text{SH}} = 7$ [16] to relate total parallel heat flux from electrons and ions to Langmuir probe measured saturation cur-

rent (J_{sat}) and electron temperature (T_e) via $q_{\parallel}^{\text{tot}} = \gamma_{\text{SH}} J_{\text{sat}} T_e / e$, close agreement is obtained between Langmuir probe measured divertor heat flux profiles and IR thermography measured heat flux profiles, as shown in Fig. A.3. The IR measurements are shown for corresponding cases where available. This agreement translates to agreement within statistical measurement uncertainty in the λ_q values inferred from Langmuir probes and IR, as shown in Fig. A.2. Importantly, the λ_q inferred from Langmuir probes is independent of the assumed γ_{SH} . Because Langmuir probes measure mainly electrons, this result can be viewed as evidence that the electron contribution to the divertor heat flux underlies the broadening of λ_q measured by IR.

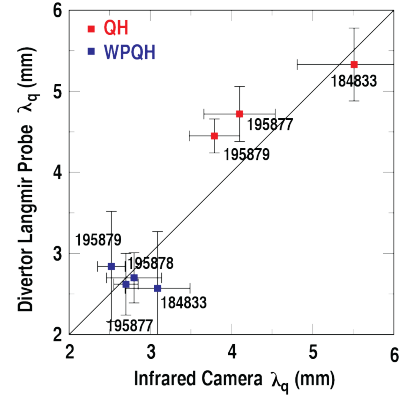
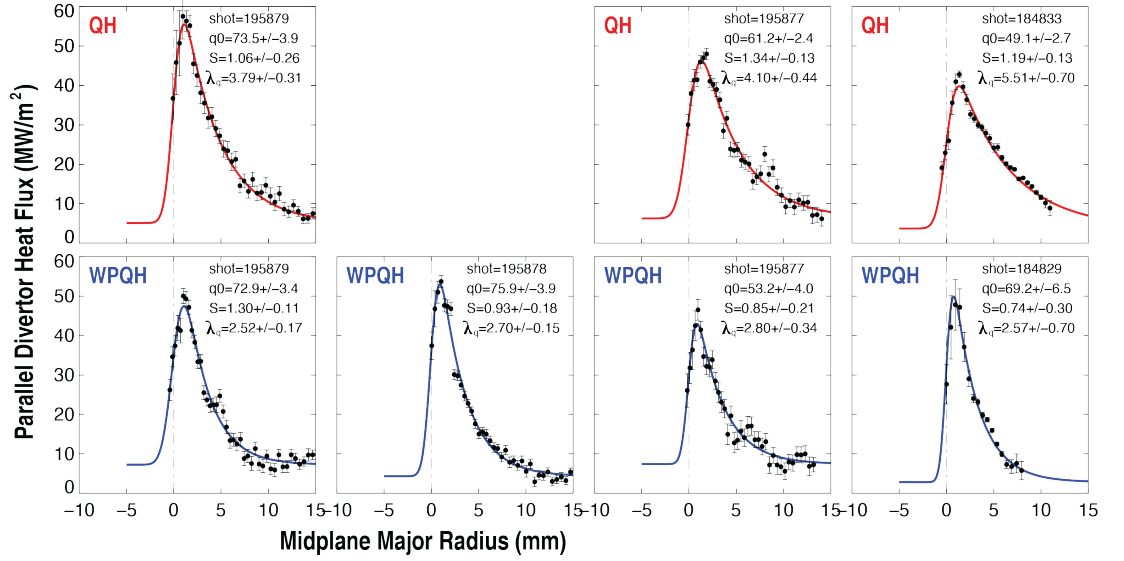


FIG. A.2. Comparison of λ_q inferred from Langmuir probe (using $\gamma_{\text{SH}} = 7$) and IR thermography.

To clarify the issue of possible heat flux sharing between the upper and lower divertors, While the overall shape is double-null characterized by two magnetic X-points, a ~ 5 mm radial separation at the midplane between their corresponding flux surfaces sends most of the heat flux to the lower divertor [22]. In all of the other, more recent, discharges used in this study the separation exceeds ~ 10 mm, which well exceeds λ_q , so that heat flux sharing should not affect the inference of λ_q .

Scaling Pedestal Turbulent Transport to Future Machines. Here we provide details on the scaling of pedestal turbulent transport with ion gyroradius, which varies inversely with magnetic field. Turbulent transport reduction by sheared flows is predicted to scale with the normalized ion gyroradius, $\rho_* = \rho_i / a$, where a is the plasma minor radius [23]. In future machines, ρ_* is expected to be approximately three times smaller than in present tokamaks. The radial electric field E_r in the edge pedestal is $Zen_i E_r \sim dp_i / dr \sim p_i / \Delta$, where Zen_i is the ion charge density, $p_i = n_i T_i$ is the ion pressure with T_i the ion temperature, r is the minor radius, and Δ is the gradient scale length. The $E \times B$ shear rate for turbulence is then $\gamma_E \sim B^{-1} dE_r / dr \sim E_r / (B\Delta)$ where B is the magnetic field. Estimating the growth rate for ion scale drift-type instabilities as $\gamma_{\text{lin}} \sim v_{\text{thi}} / \Delta$, where

Infra-Red Thermography



Divertor Langmuir Probes

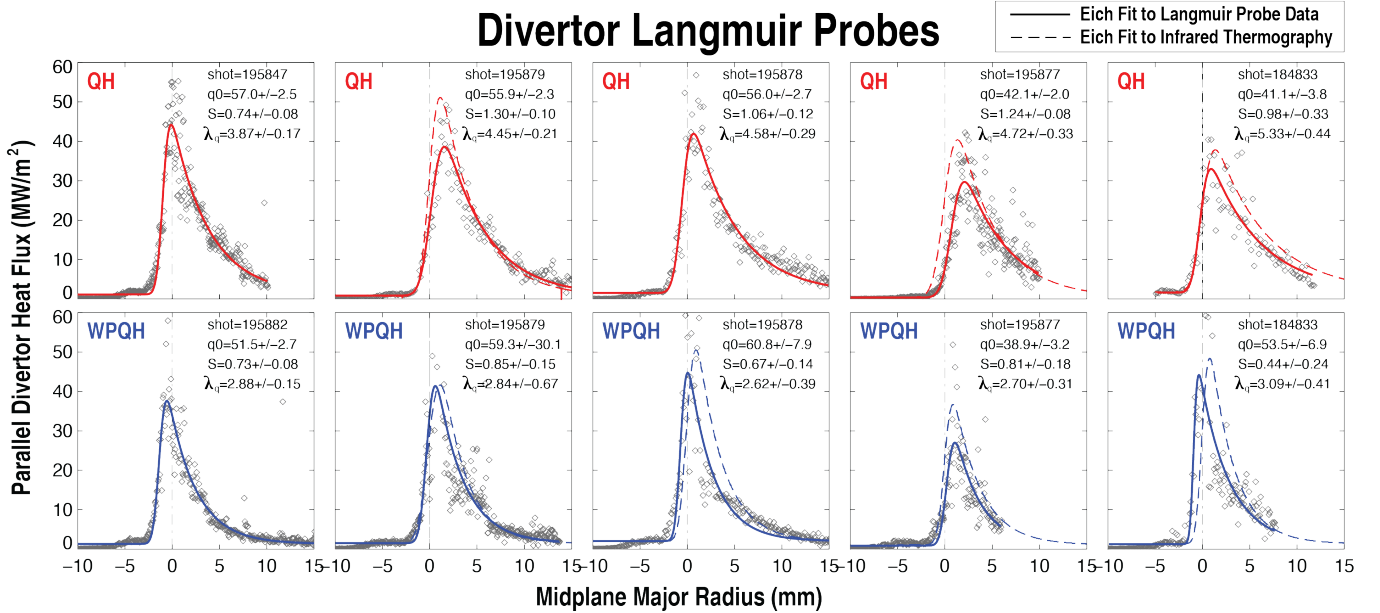


FIG. A.3. Measured parallel heat flux profiles from Infrared (IR) thermography (above, for cases where measurement is available), and Langmuir probes (below) for the discharges in Fig. 2(b). Solid lines show Eich fits with resulting parameters given in the insets. The dashed lines overlay the Eich IR fit on Langmuir probe profiles after adjusting to match q_{BG} .

$v_{\text{thi}} = (2T_i/m_i)^{1/2}$ is the ion thermal speed, the reduction of turbulent transport by $E \times B$ shear will depend on a parameter which scales as $\gamma_E/\gamma_{\text{lin}} \sim \rho_i/\Delta \sim (a/\Delta)\rho_*$. The ratio of pedestal turbulent heat flux Q to the gyroBohm flux Q_{gB} is predicted to increase asymptotically as a result of the decreased $E \times B$ shear at low ρ_* according to [24–26]

$$\frac{Q}{Q_{\text{gB}}} \sim \left(\frac{\gamma_E}{\gamma_{\text{lin}}}\right)^{-2} \sim \left(\frac{\Delta}{a}\right)^2 \frac{1}{\rho_*^2} \sim \frac{\beta_p^{2\alpha_1}}{\rho_*^2}.$$

Here $\beta_p = 8\pi p/B_p^2$ is the poloidal beta parameter, which

we have included by invoking the EPED scaling for the pedestal width as limited by the onset of kinetic ballooning modes, $\Delta \sim \beta_p^{\alpha_1}$, where $\alpha_1 \sim 0.5 - 0.75$ [13, 14]. Assuming an H-Mode pedestal is formed, pedestal turbulent transport could be approximately an order of magnitude stronger in future high magnetic field machines as a result of the factor of three reduction in ρ_* , assuming the pedestal width follows EPED scaling (KBM onset) or a “softer” version of it with $\alpha_1 < 0.75$ due to other less virulent instabilities.

* dernst@psfc.mit.edu

- [1] M. A. Makowski *et al.*, Physics of Plasmas **19**, 056122 (2012).
- [2] T. Eich *et al.*, Nucl. Fusion **53**, 93031 (2013).
- [3] R. Goldston, Nuclear Fusion **52**, 013009 (2012).
- [4] C. S. Chang *et al.*, Nuclear Fusion **57**, 116023 (2017).
- [5] C. S. Chang *et al.*, Physics of Plasmas **28**, 022501 (2021).
- [6] M. Faitsch *et al.*, Nuclear Materials and Energy **26**, 100890 (2021).
- [7] M. Faitsch *et al.*, Nuclear Fusion **63**, 076013 (2023).
- [8] T. Eich *et al.*, Nuclear Fusion **60**, 056016 (2020).
- [9] K. H. Burrell *et al.*, Physics of Plasmas **23**, 056103 (2016).
- [10] D. R. Ernst *et al.*, in *Proc. 27th IAEA Fusion Energy Conference, Gandhinagar, India, October 22 - 27, 2018* (IAEA, Vienna, 2018), paper IAEA-CN-258/EX/2-2.
- [11] K. Burrell *et al.*, Nuclear Fusion **60**, 086005 (2020).
- [12] X. Chen *et al.*, Nuclear Fusion **60**, 092006 (2020).
- [13] P. Snyder *et al.*, Nucl. Fusion **51**, 103016 (2011).
- [14] P. Snyder *et al.*, Phys. Plasmas **19**, 056115 (2012).
- [15] K. Burrell *et al.*, Phys. Plasmas **12**, 056121 (2005).
- [16] P. Stangeby, *The plasma boundary of magnetic fusion devices, Plasma Physics Series* (Institute of Physics Publishing, Bristol and Philadelphia, 2000).
- [17] G. McKee *et al.*, Rev. Sci. Instrum. **70**, 913 (1999).
- [18] D. R. Ernst *et al.*, Physics of Plasmas **23**, 056112 (2016).
- [19] J. Chen *et al.*, Rev. Sci. Instr. **87**, 11E108 (2016).
- [20] T. Evans, R. Roeder, J. Carter, and B. Rapoport, Contributions to Plasma Physics **44**, 235 (2004).
- [21] D. R. Ernst *et al.*, Bull. Am. Phys. Soc. (2022).
- [22] T. Petrie *et al.*, Nuclear Fusion **46**, 57 (2005).
- [23] M. Kotschenreuther *et al.*, in *Proc. 16th International Conference on Fusion Energy; Montreal (Canada); 7-11 Oct 1996; IAEA-CN-64/D1-5; ISSN 0074-1884* (IAEA, Vienna, 1997), pp. 371–382.
- [24] Y. Z. Zhang and S. M. Mahajan, Physics of Fluids B: Plasma Physics **4**, 1385 (1992).
- [25] M. Kotschenreuther *et al.*, Nuclear Fusion **57**, 064001 (2017).
- [26] D. R. Hatch, R. D. Hazeltine, M. K. Kotschenreuther, and S. M. Mahajan, Plasma Physics and Controlled Fusion **60**, 084003 (2018).